Loss-Induced Violation of the Fundamental Transmittance-Asymmetry Bound in Nonlinear Complex Wave Systems

Cheng-Zhen Wang[1], Rodion Kononchuk[1], Ulrich Kuhl[2], and Tsampikos Kottos[1]

[1]*Wave Transport in Complex Systems Lab, Department of Physics, Wesleyan University, Middletown, Connecticut 06459, USA*
[2]*Université Côte d'Azur, CNRS, Institut de Physique de Nice (INPHYNI), 06200, Nice, France*

Nonlinearity-induced asymmetric transport (AT) can be utilized for on-chip implementation of nonreciprocal devices that do not require odd-vector biasing. This scheme, however, is subject to a fundamental bound dictating that the maximum transmittance asymmetry is inversely proportional to the asymmetry intensity range (AIR) over which AT occurs. Contrary to the conventional wisdom, we show that the implementation of losses can lead to an increase of the AIR without deteriorating the AT. We develop a general theory that provides a new upper bound for AT in nonlinear complex systems and highlights the importance of their structural complexity and of losses. Our predictions are confirmed numerically and experimentally using a microwave complex network of coaxial cables.

Introduction.—Asymmetric or nonreciprocal devices such as isolators and circulators are routinely used in communications, radar and LIDAR technologies, and integrated photonic circuits at microwave and optical frequencies [1]. Their operational principle relies on the violation of reciprocity, which is typically achieved (in linear structures) by using an odd-vector bias (e.g., an external magnetic field) [2,3] or by violating the time invariance via a spatiotemporal modulation of the propagating medium [4–15]. Utilizing nonlinearities as a means to achieve asymmetric transport (AT) is a promising alternative approach [16–41]. In this framework, an upper bound for the maximum transmittance asymmetry has been achieved based on time-reversal symmetry considerations [34]. These studies analyze AT in simple nonlinear systems [34–37] without paying attention to the geometrical complexity of the underlying structures, nor to the presence of losses that violates time-reversal symmetry. The challenge now is to develop a general theory of nonlinearity-induced AT in typical complex wave settings that lack geometric or time-reversal symmetries.

Here, we develop a general theory of AT from complex wave scattering systems without any geometric symmetries, where nonlinearities coexist with losses. We confirm our predictions by utilizing an experimental platform of wave transport in complex systems, i.e., complex networks of coaxial cables (graphs) [42–63]; see Fig. 1(a). Specifically, we have derived a general expression for the upper bound of the transmittance asymmetry occurring in nonlinear wave media in terms of losses and other structure-specific characteristics of the underlying linear system. The necessary conditions to exceed the transmission asymmetry bound given by the corresponding lossless analogs [34–37] are identified. Furthermore, our analysis highlights an intimate relation between the AT properties of a nonlinear wave system and the structural asymmetry factor (SAF) that is determined by the geometric complexity of the underlying linear structure. We find that the SAF dictates the asymmetric intensity range (AIR) defined as the ratio of input powers injected from opposite directions which leads to the same transmittance [see Fig. 1(b)]. We demonstrate experimentally that the presence of losses does not degrade the transmission asymmetry at all—instead, it enhances the AIR.

Experimental implementation.—A nonlinear microwave graph consists of coaxial cables (bonds) coupled together via $n = 1, ..., N$ T junctions (vertices). For the tetrahedron graph shown in Fig. 1(a), $N = 4$. We have chosen the length of the bonds not to be commensurable—thus avoiding spectral degeneracies. Additionally, we made sure that our choice of bond lengths allows us to measure a sufficient number of resonances in the frequency range where the nonlinearity is activated. The local nonlinearity is always incorporated at the Nth vertex. It is implemented by substituting the T junction with a cylindrical resonator which is inductively coupled to a metallic ring that is short circuited to a diode; see inset of Fig. 1(a). The nonlinear resonator is designed to operate at 6.1–6.5 GHz. It is coupled with the rest of the graph via "kink" antennas (see Supplemental Material [64] [65]. The system is coupled to transmission lines (TLs) attached to $n = 1, 2$ vertices of the graph. Each transmission line supports a single propagating mode and it is connected to a port of the vector network analyzer.

Scattering theory for nonlinear graphs.—The theoretical analysis utilizes a standard open quantum graph description [44] with the modification that the Nth vertex is now nonlinear. We assume that the bond lengths l_B are taken
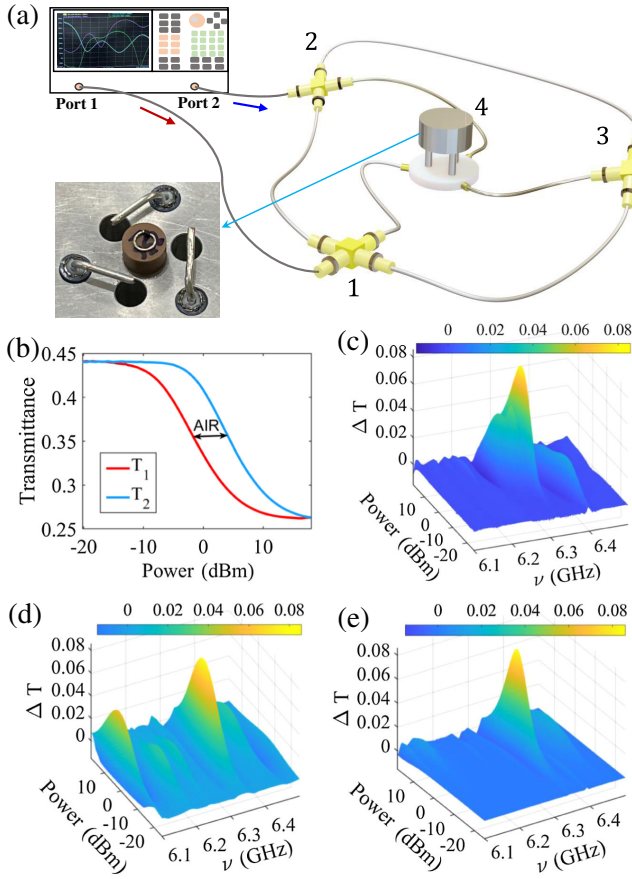
FIG. 1. (a) A microwave tetrahedron graph. The coaxial cables are connected by T or double T junctions at each of the vertices $n = 1, 2$, and 3. Vertex $N = 4$ consists of three kink antennas coupling to a cylindrical dielectric resonator that is inductively coupled to a ring antenna which is short circuited with a nonlinear diode (see left-hand inset). (b) Measured transmittance T_1 (from port 1 to port 2) and T_2 (from port 2 to port 1) at a fixed frequency ($\nu = 6.327$ GHz) as a function of the input power showing asymmetric transport. (c)–(e) The transmittance difference $\Delta T \equiv T_2 - T_1$ for an incident wave (of the same amplitude and frequency) as a function of frequency and input power. (c) Experimental data. Simulations using (d) a simple graph, and (e) a resonant-graph modeling.

from a box distribution centered around some mean value $\bar{l}$. The position $x_{nm} \equiv x$ on bond $B = (n, m)$ is $x = 0(l_B)$ on vertex $n(m)$. The scattering field on each bond satisfies the Helmholtz equation

$$\left(\frac{d^2}{dx^2} + k^2 + k^2\left(\lambda_n + \delta_{nN}f(|\phi_N^{(\alpha)}|^2)\right)\delta(x)\right)\psi_B^{(\alpha)} = 0, \quad (1)$$

where $\psi_B^{(\alpha)}(x)$ is the electric potential difference at position x, $k = \omega n_r/c$ is the wave number of the propagating wave with angular frequency ω, n_r is the relative index of refraction of the coaxial cable, c is the speed of light, λ_n is the dielectric coefficient at node n, δ_{nN} is the Kronecker

delta function, and the superscript $\alpha = 1, 2$ indicates the lead from which the incident wave has been injected. The losses in the coaxial cables are modeled by a complex-valued refraction index n_r, while losses at the vertices are modeled by complex λ_n. The scattering field $\psi_B^{(\alpha)}(x)$ is expressed in terms of its value at the vertices $\psi_B^{(\alpha)}(x = 0) = \phi_n^{(\alpha)}$ and $\psi_B^{(\alpha)}(x = l_b) = \phi_m^{(\alpha)}$. Finally, $f(|\phi_N^{(\alpha)}|^2)$ is the nonlinear dielectric coefficient at vertex N. For Kerr nonlinearities, we have $f(|\phi_N^{(\alpha)}|^2) = \chi_K|\phi_N^{(\alpha)}|^2$, while for saturable nonlinearities we have $f(|\phi_N^{(\alpha)}|^2) = z_1/[1 + \chi_s|\phi_N^{(\alpha)}|^2]$ with χ_K, χ_s, and z_1 being complex variables.

The wave function at a vertex n satisfies the continuity and the current conservation relations which can be written as (see Supplemental Material [64])

$$(M + M_{NL} + iW^T W)\Phi^{(\alpha)} = 2iW^T I^{(\alpha)}, \quad (2)$$

where we have introduced the scattering vector field $\Phi^{(\alpha)} = (\phi_1^{(\alpha)}, \phi_2^{(\alpha)}, ..., \phi_N^{(\alpha)})^T$. The two-dimensional vector $I^{(\alpha)}$ has components $I_\mu^{(\alpha)} = A_\mu\delta_{\alpha,\mu}$ and describes the amplitude of the incident field of the channel α that has been used to inject the wave. Finally, $W_{\alpha,n} = \delta_{\alpha,n}$ is a $2 \times N$ matrix describing the connection between the αth lead and the vertices $n = 1, 2$. The $N \times N$ matrix M,

$$M_{nm} = \begin{cases} \lambda_n k - \sum_{l\neq n}\mathcal{A}_{nl}\cot kL_{nl} & n = m \\ \mathcal{A}_{nm}\csc kL_{nm} & n \neq m, \end{cases} \quad (3)$$

incorporates information about the metric and the connectivity of the graph, where $\mathcal{A}$ is the adjacency matrix having elements zero (whenever two vertices are not connected) and one (whenever two vertices are connected) [44]. Finally, $(M_{NL})_{n,m} = kf(|\phi_N^{(\alpha)}|^2)\delta_{nm}\delta_{n,N}$ incorporates the nonlinearity at the $n = N$ vertex.

Using Eq. (2) we find that the field intensity at the nonlinear vertex $x_\alpha \equiv |\phi_N^{(\alpha)}|^2$ is a root of the equation (see Supplemental Material [64])

$$x_\alpha\left[|b|^2 + |kf(x_\alpha)|^2 - 2\text{Re}\left(kb^*f(x_\alpha)\right)\right] = 4|A_\alpha c_\alpha|^2, \quad (4)$$

where the coefficients $b = b(\{M_{nm}\}, \{W_{\alpha,n}\})$, and $c_\alpha = c_\alpha(\{M_{nm}\}, \{W_{\alpha,n}\})$ depend on the metric and connectivity of the *linear graph* solely, which are encoded in the matrix elements of the matrix M [see Eq. (3)], and on the coupling matrix W (for the precise definition, refer to the Supplemental Material Eqs. (SC.18) and (SC.19), respectively). In addition, c_α incorporates the information about the TL $\alpha = 1, 2$ which is used to inject the incident wave. Further manipulations allow us to turn Eq. (4) to a cubic algebraic equation for x_α which can be solved exactly using Cardano's formula (see Supplemental Material). Substituting the value of x_α back in Eq. (2) allows us to

evaluate the rest of the components of the scattering vector field $\Phi^{(\alpha)}$. Specifically, the field amplitude $\phi_{n_\beta}^{(\alpha)}$ associated with the vertex $n_\beta \neq \alpha$ is

$$\phi_{n_\beta}^{(\alpha)} = 2iA_\alpha \left[q_{\alpha\beta} - \frac{c_\alpha c_\beta}{b - kf(\mathrm{x}_\alpha)} \right], \qquad (5)$$

where the constant $q_{1,2} = q_{2,1} = q = q(\{M_{nm}\}, \{W_{\alpha,n}\})$ encodes information about the structure (metric and connectivity) of the graph and the vertices where the TLs are attached (see Supplemental Material [64]).

Evaluation of nonlinear transmittance.—The continuity condition at the vertex n enforces that the transmitted wave has the same amplitude given by Eq. (5). Consequently, the transmittance is $T_\alpha \equiv |\phi_{n_\beta}^{(\alpha)}/A_\alpha|^2$. For real-valued $f(|\phi_N^{(\alpha)}|^2)$, it takes the simple form

$$T_\alpha = 4|q|^2 \frac{\left[X_\alpha - \mathrm{Re}\left(\frac{c_1 c_2}{qk\mathrm{Im}(\frac{b}{k})}\right)\right]^2 + \left[1 - \mathrm{Im}\left(\frac{c_1 c_2}{qk\mathrm{Im}(\frac{b}{k})}\right)\right]^2}{X_\alpha^2 + 1}, \qquad (6)$$

where $X_\alpha = \{[\mathrm{Re}(b/k) - f(\mathrm{x}_\alpha)]/\mathrm{Im}(b/k)\}$ (see Supplemental Material for a generalization to complex-valued nonlinearities [64]). Figure 1(b) shows the measured transmittance T_1 (T_2) from TL 1 (2) to TL 2 (1) for a fixed frequency as a function of the input power. We find a strong nonlinear dependence of the transmissions on the input power.

Transmittance asymmetry.—Equation (6) indicate that two waves, with the same amplitude $A_1 = A_2$ and wave number k, that are injected from different ports $\alpha = 1, 2$ can lead to $T_1 \neq T_2$, provided that $X_1 \neq X_2$. The latter occurs when the roots x_α of Eq. (4) that describe the field intensities at the nonlinear vertex differ for $\alpha = 1, 2$ due to the dependence of c_α on the incident TL α [see rhs of Eq. (4)]. This nonreciprocal response does not require any form of external bias: the excitation field itself acts as a bias and triggers the system into a "high-transmission" or "low-transmission" state depending on the incident TL. In Fig. 1(c) we show the measured transmission difference $\Delta T = T_2 - T_1$ as a function of the input power and frequency ν. These measurements compare nicely with the results from the graph modeling Eqs. (2) and (3); see Fig. 1(d). More refined modeling that takes into consideration the resonant nature of the nonlinear vertex provides an even better description of the asymmetric transport; see Fig. 1(e). We will refer to it as resonant-graph modeling (see Supplemental Material [64]).

Further analysis of Eq. (4) allows us to identify the amplitude range for which asymmetric transport occurs. Specifically, from the right-hand side of this equation we conclude that the scattering field intensity x_α at the nonlinear vertex is the same for a left ($\alpha = 1$) and a right ($\alpha = 2$) incident wave as long as they satisfy the relation $|A_1 c_1|^2 = |A_2 c_2|^2$. The latter equality shows that the field

intensity x_α at the nonlinear vertex (and therefore the nonlinear electric potential) for injected waves from port 2 is equal to the one from port 1, if the input power from port 1 is $\mathrm{SAF} \equiv |c_2/c_1|^2$ times larger than that from port 2. This condition leads to the same transmission coefficients for waves injected from different ports. The ratio of these input powers that lead to the same transmission defines the $\mathrm{AIR} \equiv \max\{|A_1/A_2|^2; |A_2/A_1|^2\}$ [see Fig. 1(b)]. Within the AIR, the graph largely breaks Lorentz reciprocity, since the transmission levels in opposite directions are different for the same input power and frequency. It follows that $\mathrm{AIR} = \mathrm{SAF}$.

Bounds for transmission asymmetry.—The maximum transmittance can be used as an upper bound for the transmission asymmetry since $T \geq 0$ in all cases and, therefore, $\Delta T_{\max} = T_{\max} - T_{\min} \leq T_{\max}$.

From Eq. (6) we derive an upper bound for the transmittance by maximizing T_α with respect to X_α. For real-valued nonlinearities we have

$$T_{\max} = 2|q|^2 \Big(|\Lambda|\sqrt{|\Lambda|^2 + 4[1 - \mathrm{Im}(\Lambda)]} + |\Lambda|^2 + 2[1 - \mathrm{Im}(\Lambda)] \Big), \qquad (7)$$

where $\Lambda = \{c_1 c_2/[qk\mathrm{Im}(b/k)]\}$ (for a more general case of complex nonlinearities, see Supplemental Material [64]). Equation (7) together with Eq. (SD.10) of the Supplemental Material are the main results of this Letter. They provide guidance on the dependence of AT on the parameter Λ which encodes the structural characteristics of the graph.

The special case of lossless graph is retrieved from the above expression for $\mathrm{Im}(\Lambda) = 1$ (see Supplemental Material). In this case, Eq. (7) simplifies to

$$T_{\max} = \frac{4 \times \mathrm{SAF}}{(\mathrm{SAF} + 1)^2}. \qquad (8)$$

This expression is nicely confirmed from our numerical data for a lossless graph with Kerr (open blue circles) and saturable nonlinearities (not shown) in Fig. 2(a). A further investigation reveals that there is an interlinked relation between the maximum transmittance achieved for a specific incident power and the SAF (or equivalently of the AIR [34,36,37]). This is reflected in the three examples shown in the inset of Fig. 2(a), where we report the transmittances T_1, T_2 associated with the same incident wave being injected from channels $\alpha = 1$ and $\alpha = 2$, respectively, versus the incident power. We find that an increase in the AIR (=SAF) is associated with a decrease in the maximum transmittance and vice versa as expected by Eq. (8).

Necessary conditions for the violation of an upper bound for asymmetric transport.—Equation (8) has been previously derived as the upper bound of nonlinear AT. Its
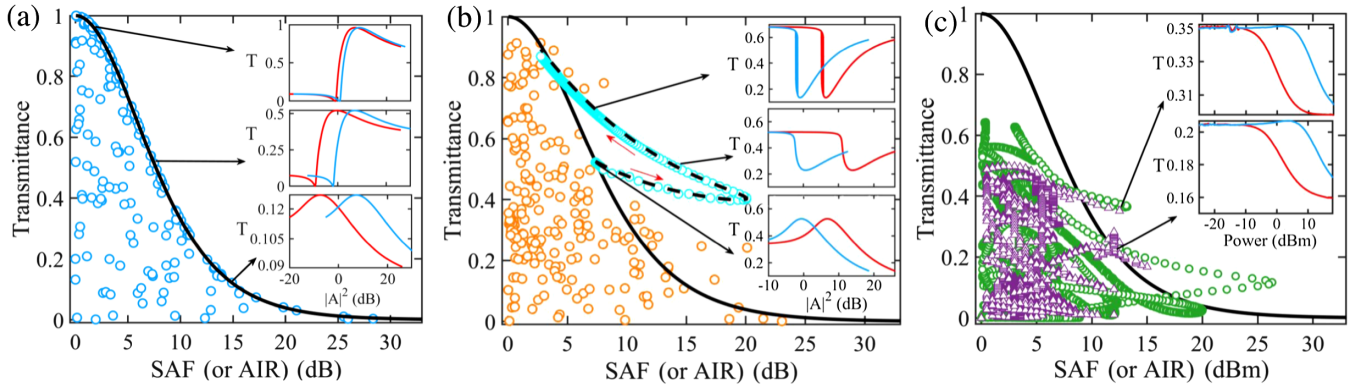
FIG. 2. Transmittance versus structural asymmetry factor (SAF) or asymmetric intensity range (AIR). (a) Lossless graph. The insets show the transmittances versus input intensity from each of the two leads (red and blue lines) for three different SAF graph configurations. (b) Lossy graph with losses on node $n_0 = 3$. The light blue circles indicate maximum transmittance for a graph configuration with increasing loss (along the direction of the red arrow) on node 3. The insets correspond to different losses for a fixed graph configuration. (c) Measurements (purple triangles) and simulations (green circles) for an ensemble of graphs with bond losses and a lossy saturable nonlinearity. The ensemble has been generated by interchanging the bonds of the graph. The insets show measurements corresponding to the same SAF but different maximum transmission values. The black solid and dashed lines in (a)–(c) are theoretical predictions while the colored circles are simulations occurring at various wavelengths and graph configurations. The data acquisition has been performed for three different graph configurations and for a frequency range $\nu \in [6.1 \text{ GHz}, 6.5 \text{ GHz}]$ with a resolution of $\delta\nu = 0.4$ MHz.

derivation assumed nonlinear Fano resonators with time-reversal symmetry (i.e., no losses) and has utilized the coupled-mode theory framework [34,36,66]. Here, however, we have derived Eq. (8) for a generic nonlinear wave system, where SAF explicitly refers to specific bulk asymmetries pertaining to the topology and metrics of the graph. Given the technological importance of AT, it is natural to investigate and establish (necessary) conditions which enforce the violation of Eq. (8) and allow for an enhanced AIR (for a fixed $T_{\max}$) or enhanced transmission asymmetry bound (for a fixed AIR) given by Eq. (7).

As discussed above, Eq. (8) does not hold when losses are introduced in the system. However, the lossy elements need to be strategically placed either on the bonds of the graph or at vertices not connected to the two TLs or the nonlinear vertex; i.e., $n_{\text{loss}} \neq 1, 2, N$ (see Supplemental Material [64]). In the opposite case of losses located at the nonlinear vertex, a simple renormalization of the nonlinearity (so that it incorporates the lossy term) results in an upper bound given by Eq. (8). Similarly, when the losses are implemented on a vertex connected to the TLs, a new bound is found which is a stricter version of Eq. (8) (see Supplemental Material).

We find that the interference between (at least) two nearby resonance modes can result in a violation of Eq. (8) as in the case of AT due to the presence of a magnetic field [67] (see Supplemental Material). Finally, from Eq. (7) we speculate that if $\text{Im}(\Lambda) < 1$, the lossy graph configurations might violate the lossless bound given by Eq. (8). Detailed numerical analysis has confirmed that the above inequality is a necessary but not sufficient condition for violating the lossless limit (see Supplemental Material [64]).

A numerical example where the violation of Eq. (8) occurs for a tetrahedron graph with losses at the vertex $n_0 = 3$ is shown in Fig. 2(b). Such targeted arrangement of loss is effectively equivalent to a new graph configuration where a third (fictitious) channel is attached to the node n_0, thus changing the topology of the graph and indirectly affecting the coupling between this vertex and the other vertices. While Eq. (8) is violated for intermediate values of loss, it is still respected in the two limiting cases of zero and very large losses at the n_0 vertex. The second limit is understood as an impedance-mismatch phenomenon: due to the large imaginary "electric potential," the n_0 vertex is decoupled from the rest of the graph, which now acts as a lossless system with $N - 1$ vertices and thus again satisfies the bound of Eq. (8). In Fig. 2(b) we demonstrate the trajectory of the maximum transmittance versus AIR as the losses at the vertex $n_0 = 3$ of a tetrahedron graph increase. The numerical data (light blue cycles) for $T_{\max}$ nicely match the theoretical results (dashed black line) of Eq. (7), indicating that the deterioration of $T_{\max}$ for increasing losses occurs at a slower rate than the enhancement of AIR. At some loss strength, the AIR reaches its maximum value. Further increase of loss results in a decrease (increase) of AIR ($T_{\max}$) toward its "impedance-mismatch" limit.

In Fig. 2(c) we report our measurements (purple triangles) for the graph of Fig. 1, with uniformly distributed losses at the bonds of the graph. A violation of Eq. (8) is evident and it is qualitatively supported by our simulations (green cycles) using a resonant-graph modeling for the same bond configurations. The difference between the simulations and the experiment is primarily due to dispersion in the real and imaginary part of the refraction index and other loss sources, such as the T junctions, which have not been taken into account. The insets in Fig. 2(c)
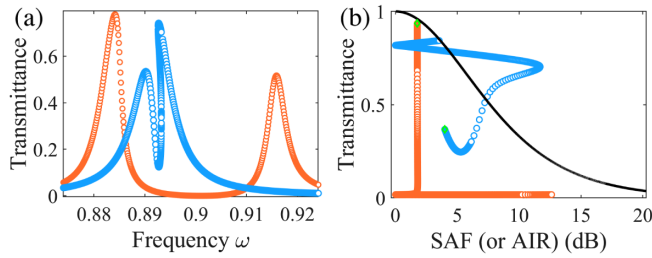
FIG. 3. (a) Two examples of overlapping (blue circles) and isolated (orange circles) resonance scenarios using NLRMT modeling. (b) The (maximum) transmittance versus SAF for the two cases shown in (a) for a fixed value of the frequency ($\omega = 0.884$ for the isolated resonance case and $\omega = 0.892$ for the overlapping resonance case) of the incident wave. The loss increases from zero (green diamonds). The system that supports overlapping resonances breaks the lossless bound Eq. (8) (solid black line) at certain loss values. For details see Supplemental Material Sec. J [64].

report the experimental transmittances T_1, T_2 for two cases with the same SAF—the upper one exceeds the bound, while the lower case corresponds to a configuration that respects the bound (see black arrows).

All the above conclusions have been further confirmed by a nonlinear random matrix theory (NLRMT) which can model typical nonlinear chaotic cavities (see Supplemental Material [64]). An example of the violation of Eq. (8) for overlapping resonances is shown in Fig. 3.

Conclusions.—Using a generic nonlinear complex wave system, we have established experimentally and theoretically an exact expression for the upper bound of transmittance asymmetry in the presence of losses. We have identified necessary conditions for enhanced asymmetry intensity range (for a fixed $T_{\max}$) or enhanced transmission-asymmetry bound (for a fixed AIR). It will be interesting to extend these studies toward a universal statistical description of transmission asymmetries using NLRMT. Another interesting direction would be the derivation of the bounds Eqs. (7) and (8) in the case of microwave graphs using semiclassical tools. This will allow us to unveil the influence of nonuniversal features (e.g., wave scars), which are present in any typical dynamical system, to the non-linearity-induced AT.

[1] C. Caloz, A. Alù, S. Tretyakov, D. Sounas, K. Achouri, and Z.-L. Deck-Léger, Electromagnetic Nonreciprocity, Phys. Rev. Appl. **10**, 047001 (2018).

[2] D. M. Pozar, *Microwave Engineering* (John Wiley & Sons, New York, 2011).

[3] R. J. Potton, Reciprocity in optics, Rep. Prog. Phys. **67**, 717 (2004).

[4] Z. Yu and S. Fan, Complete optical isolation created by indirect interband photonic transitions, Nat. Photonics **3**, 91 (2009).

[5] K. Fang, Z. Yu, and S. Fan, Realizing effective magnetic field for photons by controlling the phase of dynamic modulation, Nat. Photonics **6**, 782 (2012).

[6] K. Fang, Z. Yu, and S. Fan, Photonic Aharonov-Bohm Effect Based on Dynamic Modulation, Phys. Rev. Lett. **108**, 153901 (2012).

[7] H. Lira, Z. Yu, S. Fan, and M. Lipson, Electrically Driven Nonreciprocity Induced by Interband Photonic Transition on a Silicon Chip, Phys. Rev. Lett. **109**, 033901 (2012).

[8] D.-W. Wang, H.-T. Zhou, M.-J. Guo, J.-X. Zhang, J. Evers, and S.-Y. Zhu, Optical Diode Made from a Moving Photonic Crystal, Phys. Rev. Lett. **110**, 093901 (2013).

[9] D. L. Sounas, C. Caloz, and A. Alù, Giant non-reciprocity at the subwavelength scale using angular momentum-biased metamaterials, Nat. Commun. **4**, 2407 (2013).

[10] R. Fleury, D. L. Sounas, C. F. Sieck, M. R. Haberman, and A. Alù, Sound isolation and giant linear nonreciprocity in a compact acoustic circulator, Science **343**, 516 (2014).

[11] L. D. Tzuang, K. Fang, P. Nussenzveig, S. Fan, and M. Lipson, Non-reciprocal phase shift induced by an effective magnetic flux for light, Nat. Photonics **8**, 701 (2014).

[12] N. A. Estep, D. L. Sounas, J. Soric, and A. Alù, Magnetic-free non-reciprocity and isolation based on parametrically modulated coupled-resonator loops, Nat. Phys. **10**, 923 (2014).

[13] F. Ruesink, M.-A. Miri, A. Alù, and E. Verhagen, Non-reciprocity and magnetic-free isolation based on optome-chanical interactions, Nat. Commun. **7**, 13662 (2016).

[14] D. B. Sohn, S. Kim, and G. Bahl, Time-reversal symmetry breaking with acoustic pumping of nanophotonic circuits, Nat. Photonics **12**, 91 (2018).

[15] D. L. Sounas and A. Alù, Non-reciprocal photonics based on time modulation, Nat. Photonics **11**, 774 (2017).

[16] K. Gallo, G. Assanto, K. R. Parameswaran, and M. M. Fejer, All-optical diode in a periodically poled lithium niobate waveguide, Appl. Phys. Lett. **79**, 314 (2001).

[17] H. Zhou, K.-F. Zhou, W. Hu, Q. Guo, S. Lan, X.-S. Lin, and A. Venu Gopal, All-optical diodes based on photonic crystal molecules consisting of nonlinear defect pairs, J. Appl. Phys. **99**, 123111 (2006).

[18] X.-S. Lin, W.-Q. Wu, H. Zhou, K.-F. Zhou, and S. Lan, Enhancement of unidirectional transmission through the coupling of nonlinear photonic crystal defects, Opt. Express **14**, 2429 (2006).

[19] S. Manipatruni, J. T. Robinson, and M. Lipson, Optical Nonreciprocity in Optomechanical Structures, Phys. Rev. Lett. **102**, 213903 (2009).

[20] A. E. Miroshnichenko, E. Brasselet, and Y. S. Kivshar, Reversible optical nonreciprocity in periodic structures with liquid crystals, Appl. Phys. Lett. 96, 26 (2010).

[21] S. V. Zhukovsky and A. G. Smirnov, All-optical diode action in asymmetric nonlinear photonic multilayers with perfect transmission resonances, Phys. Rev. A 83, 023818 (2011).

[22] I. V. Shadrivov, V. A. Fedotov, D. A. Powell, Y. S. Kivshar, and N. I. Zheludev, Electromagnetic wave analogue of an electronic diode, New J. Phys. 13, 033025 (2011).

[23] S. Lepri and G. Casati, Asymmetric Wave Propagation in Nonlinear Systems, Phys. Rev. Lett. 106, 164101 (2011).

[24] W. Ding, B. Luk'yanchuk, and C.-W. Qiu, Ultrahigh-contrast-ratio silicon Fano diode, Phys. Rev. A 85, 025806 (2012).

[25] L. Fan, J. Wang, L. T. Varghese, H. Shen, B. Niu, Y. Xuan, A. M. Weiner, and M. Qi, An all-silicon passive optical diode, Science 335, 447 (2012).

[26] B. Anand, R. Podila, K. Lingam, S. Krishnan, S. Siva Sankara Sai, R. Philip, and A. M. Rao, Optical diode action from axially asymmetric nonlinearity in an all-carbon solid-state device, Nano Lett. 13, 5771 (2013).

[27] N. Bender, S. Factor, J. D. Bodyfelt, H. Ramezani, D. N. Christodoulides, F. M. Ellis, and T. Kottos, Observation of Asymmetric Transport in Structures with Active Nonlinearities, Phys. Rev. Lett. 110, 234101 (2013).

[28] F. Nazari, N. Bender, H. Ramezani, M. Moravvej-Farshi, D. Christodoulides, and T. Kottos, Optical isolation via $\mathcal{PT}$-symmetric nonlinear Fano resonances, Opt. Express 22, 9574 (2014).

[29] B. Peng, Ş. K. Özdemir, F. Lei, F. Monifi, M. Gianfreda, G. L. Long, S. Fan, F. Nori, C. M. Bender, and L. Yang, Parity–time-symmetric whispering-gallery microcavities, Nat. Phys. 10, 394 (2014).

[30] Y. Xu and A. E. Miroshnichenko, Reconfigurable non-reciprocity with a nonlinear Fano diode, Phys. Rev. B 89, 134306 (2014).

[31] A. M. Mahmoud, A. R. Davoyan, and N. Engheta, All-passive nonreciprocal metastructure, Nat. Commun. 6, 8359 (2015).

[32] Y. Yu, Y. Chen, H. Hu, W. Xue, K. Yvind, and J. Mork, Nonreciprocal transmission in a nonlinear photonic-crystal Fano structure with broken symmetry, Laser Photonics Rev. 9, 241 (2015).

[33] M. Lawrence, D. R. Barton III, and J. A. Dionne, Nonreciprocal flat optics with silicon metasurfaces, Nano Lett. 18, 1104 (2018).

[34] D. L. Sounas and A. Alù, Fundamental bounds on the operation of Fano nonlinear isolators, Phys. Rev. B 97, 115431 (2018).

[35] D. L. Sounas, J. Soric, and A. Alù, Broadband passive isolators based on coupled nonlinear resonances, National Electron. 1, 113 (2018).

[36] M. Cotrufo, S. A. Mann, H. Moussa, and A. Alù, Non-linearity-induced nonreciprocity—Part I, IEEE Trans. Microwave Theory Tech. 69, 3569 (2021).

[37] M. Cotrufo, S. A. Mann, H. Moussa, and A. Alù, Non-linearity-induced nonreciprocity—Part II, IEEE Trans. Microwave Theory Tech. 69, 3584 (2021).

[38] K. Y. Yang, J. Skarda, M. Cotrufo, A. Dutt, G. H. Ahn, M. Sawaby, D. Vercruysse, A. Arbabian, S. Fan, A. Alù et al., Inverse-designed non-reciprocal pulse router for chip-based LiDAR, Nat. Photonics 14, 369 (2020).

[39] A. Mekawy, D. L. Sounas, and A. Alù, Free-space non-reciprocal transmission based on nonlinear coupled Fano metasurfaces, Photonics 8, 139 (2021).

[40] D. M. Solís and N. Engheta, Nonreciprocal Epsilon-Near-Zero-Dielectric Bilayers: Enhancement of Nonreciprocity from a Nonlinear Transparent Conducting Oxide Thin Film at Epsilon-Near-Zero Frequency, Phys. Rev. Appl. 17, 034053 (2022).

[41] M. Cotrufo, A. Cordaro, D. L. Sounas, A. Polman, and A. Alù, Passive bias-free nonreciprocal metasurfaces based on nonlinear quasi-bound states in the continuum, arXiv:2210.05586.

[42] T. Kottos and U. Smilansky, Quantum Chaos on Graphs, Phys. Rev. Lett. 79, 4794 (1997).

[43] T. Kottos and U. Smilansky, Periodic orbit theory and spectral statistics for quantum graphs, Ann. Phys. (N.Y.) 274, 76 (1999).

[44] T. Kottos and U. Smilansky, Chaotic Scattering on Graphs, Phys. Rev. Lett. 85, 968 (2000).

[45] C. Texier and G. Montambaux, Scattering theory on graphs, J. Phys. A 34, 10307 (2001).

[46] T. Kottos and U. Smilansky, Quantum graphs: A simple model for chaotic scattering, J. Phys. A 36, 3501 (2003).

[47] H. Schanz and T. Kottos, Scars on Quantum Networks Ignore the Lyapunov Exponent, Phys. Rev. Lett. 90, 234101 (2003).

[48] S. Gnutzmann and A. Altland, Universal Spectral Statistics in Quantum Graphs, Phys. Rev. Lett. 93, 194101 (2004).

[49] S. Gnutzmann and U. Smilansky, Quantum graphs: Applications to quantum chaos and universal spectral statistics, Adv. Phys. 55, 527 (2006).

[50] S. Gnutzmann, J. P. Keating, and F. Piotet, Quantum Ergodicity on Graphs, Phys. Rev. Lett. 101, 264102 (2008).

[51] Z. Pluhař and H. A. Weidenmüller, Universal Chaotic Scattering on Quantum Graphs, Phys. Rev. Lett. 110, 034101 (2013).

[52] Z. Pluhař and H. A. Weidenmüller, Universal Quantum Graphs, Phys. Rev. Lett. 112, 144102 (2014).

[53] F. Haake, S. Gnutzmann, and M. Kuś, Quantum Signatures of Chaos, Springer Series in Synergetics (Springer Berlin, Heidelberg, 2018), 10.1007/978-3-642-05428-0.

[54] O. Hul, S. Bauch, P. Pakoński, N. Savytskyy, K. Życzkowski, and L. Sirko, Experimental simulation of quantum graphs by microwave networks, Phys. Rev. E 69, 056205 (2004).

[55] M. Ławniczak, O. Hul, S. Bauch, P. Seba, and L. Sirko, Experimental and numerical investigation of the reflection coefficient and the distributions of Wigner's reaction matrix for irregular graphs with absorption, Phys. Rev. E 77, 056210 (2008).

[56] M. Ławniczak, S. Bauch, O. Hul, and L. Sirko, Experimental investigation of the enhancement factor for microwave irregular networks with preserved and broken time reversal symmetry in the presence of absorption, Phys. Rev. E 81, 046204 (2010).

[57] M. Białous, V. Yunko, S. Bauch, M. Ławniczak, B. Dietz, and L. Sirko, Power Spectrum Analysis and Missing Level

Statistics of Microwave Graphs with Violated Time Reversal Invariance, Phys. Rev. Lett. **117,** 144101 (2016).

[58] A. Rehemanjiang, M. Allgaier, C. H. Joyner, S. Müller, M. Sieber, U. Kuhl, and H.-J. Stöckmann, Microwave Realization of the Gaussian Symplectic Ensemble, Phys. Rev. Lett. **117,** 064101 (2016).

[59] B. Dietz, V. Yunko, M. Białous, S. Bauch, M. Ławniczak, and L. Sirko, Nonuniversality in the spectral properties of time-reversal-invariant microwave networks and quantum graphs, Phys. Rev. E **95,** 052202 (2017).

[60] J. Lu, J. Che, X. Zhang, and B. Dietz, Experimental and numerical investigation of parametric spectral properties of quantum graphs with unitary or symplectic symmetry, Phys. Rev. E **102,** 022309 (2020).

[61] L. Chen, T. Kottos, and S. M. Anlage, Perfect absorption in complex scattering systems with or without hidden symmetries, Nat. Commun. **11,** 1 (2020).

[62] L. Chen, S. M. Anlage, and Y. V. Fyodorov, Statistics of Complex Wigner Time Delays as a Counter of s-Matrix Poles: Theory and Experiment, Phys. Rev. Lett. **127,** 204101 (2021).

[63] J. Che, X. Zhang, W. Zhang, B. Dietz, and G. Chai, Fluctuation properties of the eigenfrequencies and scattering matrix of closed and open unidirectional graphs with chaotic wave dynamics, Phys. Rev. E **106,** 014211 (2022).

[64] See Supplemental Material at http://link.aps.org/supplemental/10.1103/PhysRevLett.131.123801 for details on the experimental setup, the characterization of the nonlinearity, different kind of modellings.

[65] D. H. Jeon, M. Reisner, F. Mortessagne, T. Kottos, and U. Kuhl, Non-Hermitian CT-Symmetric Spectral Protection of Nonlinear Defect Modes, Phys. Rev. Lett. **125,** 113901 (2020).

[66] D. L. Sounas and A. Alù, Time-Reversal Symmetry Bounds on the Electromagnetic Response of Asymmetric Structures, Phys. Rev. Lett. **118,** 154302 (2017).

[67] B. Dietz, T. Friedrich, H. L. Harney, M. Miski-Oglu, A. Richter, F. Schäfer, and H. A. Weidenmüller, Induced Time-Reversal Symmetry Breaking Observed in Microwave Billiards, Phys. Rev. Lett. **98,** 074103 (2007).